

# Efficient 3D FDTD analysis of arbitrary birefringent and dichroic media with obliquely incident sources

Matthew N. Miskiewicz, Patrick T. Bowen, and Michael J. Escuti

North Carolina State Univ, Dept Electrical & Computer Engineering, Raleigh, NC (USA)

## ABSTRACT

We have developed a 3D Finite Difference Time Domain (FDTD) algorithm to model obliquely incident waves through arbitrary birefringent and dichroic media with transverse periodic boundaries. Beginning with arbitrary conductivity and permittivity tensors, we employed the split-field method (SFM) to enable broadband sources with oblique incidence. We terminate our boundaries with a uniaxial perfectly matched layer (UPML) in one dimension and periodic boundaries in the other two dimensions. The algorithm is validated via several case studies: a polarizer pair, a twisted nematic liquid crystal, and an array of conducting particles. Using this approach, we simulate for the first time polarization gratings with light obliquely incident in directions orthogonal to the grating vector (i.e., at oblique angles outside the normal diffraction plane).

**Keywords:** FDTD, 3D, oblique incidence, birefringence, dichroism, split-field

## 1. INTRODUCTION

In 1966, Yee proposed a numerical method of solving Maxwell's equations by continuously stepping forward in time in discrete steps and solving a series of linear equations at each step.<sup>1</sup> The method became known as the Finite Difference Time Domain Method (FDTD), and has proven an extremely useful tool for modeling of electromagnetic radiation. It can be used to determine the broadband optical response of a device, as well as the electric and magnetic field behavior within and around a given structure. Being a numerical method, FDTD is capable of simulating arbitrarily complex structures that purely analytic methods are incapable of.

Over the years, there have been dozens of improvements upon the basic FDTD scheme, motivated by the growth of telecommunication, optics/photonics, and nano-electronics. Some developments, such as non-orthogonal coordinate systems<sup>2</sup> and reflectionless absorbing boundary conditions,<sup>3</sup> have been generally applicable and allow for either faster or more accurate computation. Other techniques fundamentally advanced the simulation capabilities of FDTD, such as the modeling of dispersive<sup>4</sup> or anisotropic media.<sup>5</sup>

The Split-Field Method (SFM) is a version of FDTD, pioneered by Roden et al.,<sup>6</sup> as a way of simulating obliquely incident plane wave sources with periodic media. The SFM allows oblique incidence study of devices such as diffractive optics,<sup>7</sup> antennas,<sup>8</sup> and photonic band gap structures.<sup>6</sup> Oh et al. developed a version of the SFM for simulating anisotropic materials, limited to structures inhomogeneous in two dimensional and with real permittivity tensors (i.e., no conductivity).<sup>7</sup> Such a method is highly desirable for understanding complex anisotropic thin-film devices, such as liquid crystal display geometries and birefringent diffraction gratings. While both the extended Jones matrix method<sup>9</sup> and the Berreman 4x4 method<sup>10</sup> can model oblique incidence anisotropic structures, they are strictly limited by specific types of geometries and their ability to model wave interaction phenomena. It is in these areas that FDTD excels.

In this paper, we propose a new FDTD algorithm based on the SFM that allows broadband simulations of structures inhomogeneous in three dimensions with arbitrary permittivity and conductivity tensors. To our knowledge, this is the first time a 3D oblique incidence FDTD method with arbitrary anisotropic media has been put forth. This algorithm is attractive because it allows us to simulate elements such as 3D diffractive optics, metallic gratings, photonic crystals, and complex birefringent and dichroic media. We validate the algorithm through three numerical samples: a pair of crossed polarizers, a twisted nematic liquid crystal cell, and an array of conducting particles. We then use the method to analyze a polarization grating (PG) at arbitrary oblique incidence. A PG is a thin-film diffractive optical element capable of diffracting light to single diffraction orders with near 100% efficiency.<sup>11</sup> All PGs have an optical axis which periodically rotates as a linear function of distance, making them a highly anisotropic and inhomogeneous structure.

---

Correspondence should be sent to: mjescuti@ncsu.edu, Telephone: +1 919 513 7363

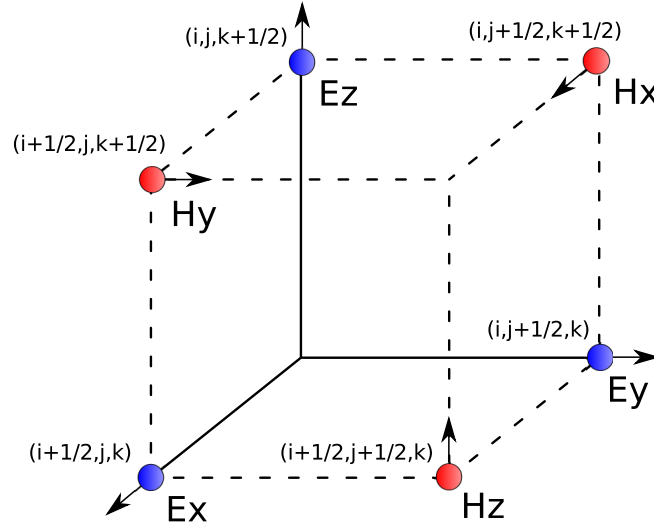


Figure 1: E and H field spatial placement within the traditional Yee Cell, which simplifies the curl operations.

## 2. BACKGROUND

### 2.1 FDTD Review

The conventional spatial arrangement of the  $\mathbf{E}$  and  $\mathbf{H}$  fields, called the Yee Cell, is shown in Fig. 1. In the Yee Cell, the orthogonal vector components of  $\mathbf{E}$  and  $\mathbf{H}$  are spatially distinct. This arrangement has the convenient property of simplifying the finite difference form of the curl operator. Our algorithm uses the Yee Cell for simplicity and efficiency.

Fig. 2 shows the problem space for a typical FDTD simulation of periodic media. The source is a plane wave excited in the entire  $\hat{x} - \hat{y}$  plane that propagates in the  $\hat{z}$  directions. The  $\hat{z}$  boundaries of the computation space are terminated with PML that eliminate exiting waves without producing reflections that would interfere with the simulation. In this paper we will use a specific PML called the Uniaxial PML (UPML).<sup>3</sup> We must terminate the  $\hat{x}$  and  $\hat{y}$  boundaries with periodic boundary conditions (PBC), which are easily implemented.

For normal incidence sources, these PBC work very well. However, for oblique incidence broadband (pulsed) sources, the PBC fail because of a phase difference between the two sides of the problem space. The SFM has been developed as a highly successful solution to this problem.<sup>6</sup> In the SFM, the electric and magnetic fields are transformed into new field variables such that the phase difference between the two sides of the problem space is eliminated and the PBC work as desired.

### 2.2 Mathematical Basis

The FDTD method is a numerical embodiment of Maxwell's equations. Physical phenomena such as interference and evanescent waves will appear in FDTD simulations without any extra effort. This is very useful, as many optical phenomena either difficult or impossible to model in analytic methods will be readily present in FDTD. The range of physical phenomena which an FDTD algorithm can emulate is a result of how precisely Maxwell's equations are implemented. For our purposes, we will consider Maxwell's equations for anisotropic nonmagnetic materials, expressed fully using permittivity and conductivity tensors, given in Eq. (1).

$$\frac{\partial}{\partial t}(\epsilon_0 \epsilon \mathbf{E}) + \boldsymbol{\sigma} \mathbf{E} = \nabla \times \mathbf{H} \quad (1a)$$

$$\frac{\partial}{\partial t}(\mu_0 \boldsymbol{\mu} \mathbf{H}) = -\nabla \times \mathbf{E} \quad (1b)$$

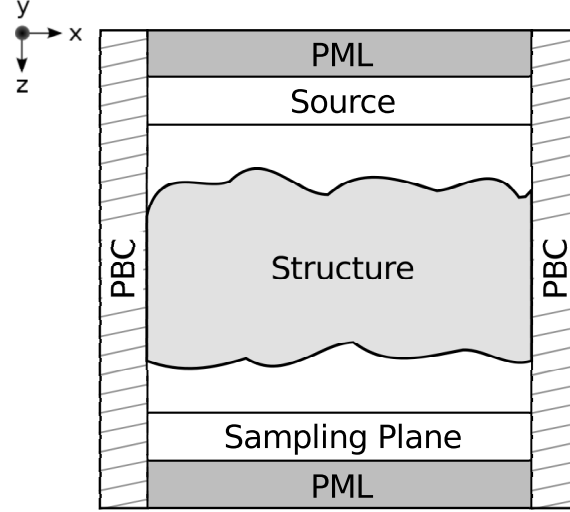


Figure 2: General problem space for FDTD simulations used in this paper. The problem space in the  $\hat{x} - \hat{z}$  plane is shown, which is identical the that of the  $\hat{y} - \hat{z}$  plane.

An anisotropic material is specified completely with full permittivity ( $\epsilon$ ) and conductivity ( $\sigma$ ) tensors. These tensors can be obtained by rotating any body with linear dielectric and conductive properties according to Euler angles.<sup>12</sup> The relative permeability tensor  $\mu$  is unity for nonmagnetic materials and therefore ignored. Since the time derivatives in Eq. (1) are to be exploited for the FDTD method, the tensors are consolidated away from the left hand side. In phasor form, Eq. (1) becomes

$$j\omega\epsilon_0\mathbf{E} + \boldsymbol{\sigma}'\mathbf{E} = \boldsymbol{\kappa}\nabla \times \mathbf{H} \quad (2a)$$

$$j\omega\mu_0\mathbf{H} = -\nabla \times \mathbf{E} \quad (2b)$$

where we have substituted  $\boldsymbol{\kappa} = \epsilon^{-1}$  as the impermittivity, and  $\boldsymbol{\sigma}' = \boldsymbol{\kappa} \cdot \boldsymbol{\sigma}$ . Eq. (2) is the core equation for our FDTD algorithm.

### 3. APPROACH

#### 3.1 The Split-Field Method With Full Tensor Descriptions

The SFM is implemented by making a variable substitution for the electric and magnetic fields such that the new variables are aligned with the periodic boundaries. We first define a plane wave propagating in the  $\mathbf{k}$  direction, using

$$\mathbf{k} = k_x\hat{x} + k_y\hat{y} + k_z\hat{z} = \frac{\omega}{c}(\sin(\theta)\cos(\psi)\hat{x} + \sin(\theta)\sin(\psi)\hat{y} + \cos(\theta)\hat{z}) \quad (3)$$

where we use  $\theta$ , the polar angle from the  $\hat{z}$  axis, and  $\phi$ , the azimuthal angle from the  $\hat{x}$  axis, to define the wave-vector  $\mathbf{k}$ .<sup>8</sup> Using  $\mathbf{k}$ , we define the new field variables  $\mathbf{P}$  and  $\mathbf{Q}$  which implicitly contain the oblique field propagation:

$$\mathbf{P} = \mathbf{E}e^{j(k_x x + k_y y)} \quad (4a)$$

$$\mathbf{Q} = c\mu_0\mathbf{H}e^{j(k_x x + k_y y)}. \quad (4b)$$

Substituting Eq. (4) into Eq. (2), we obtain:

$$\frac{j\omega}{c}\mathbf{P} + \mu_0 c \sigma' \mathbf{P} = \kappa \nabla \times \mathbf{Q} + \frac{j\omega}{c} \kappa \mathbf{q} \mathbf{Q} \quad (5a)$$

$$\frac{j\omega}{c} \mathbf{Q} = -\nabla \times \mathbf{P} - \frac{j\omega}{c} \mathbf{q} \mathbf{P}. \quad (5b)$$

In order to maintain our matrix formalism, we have defined a matrix  $\mathbf{q}$ . The matrix  $\mathbf{q}$  multiplied by a split-field vector represents the constant terms of the vector produced by the curl operator in Eq. (2). If the SFM is applied in a different coordinate system (e.g. a non-orthogonal grid), then a corresponding  $\mathbf{q}$  matrix can be defined to represent the resulting constant  $\mathbf{Q}$  and  $\mathbf{P}$  terms. As an example, in our three dimensional case this results in the following  $\mathbf{q}$  matrix:

$$\mathbf{q} = \frac{c}{\omega} \begin{bmatrix} 0 & 0 & -k_y \\ 0 & 0 & k_x \\ k_y & -k_x & 0 \end{bmatrix}. \quad (6)$$

Because there is a time derivative on each side of Eq. (5), it cannot be put directly into finite difference form. We therefore define a new set of variables to remove the time derivative on the right hand side, separating the  $\mathbf{P}$  and  $\mathbf{Q}$  fields into two components.

$$\mathbf{P} = \mathbf{P}_a + \kappa \mathbf{q} \mathbf{Q} \quad (7a)$$

$$\mathbf{Q} = \mathbf{Q}_a - \mathbf{q} \mathbf{P} \quad (7b)$$

Substituting Eq. (7) into Eq. (5) and discretizing the equation with respect to time gives:

$$\frac{1}{c\Delta t} [\mathbf{P}_a^{n+1} - \mathbf{P}_a^n] = \kappa \nabla \times \mathbf{Q}^{n+1/2} - c\mu_0 \sigma' (\kappa \mathbf{q} \mathbf{Q}^{n+1/2} + \mathbf{P}_a^{n+1/2}) \quad (8a)$$

$$\frac{1}{c\Delta t} [\mathbf{Q}_a^{n+1} - \mathbf{Q}_a^n] = -\nabla \times \mathbf{P}^{n+1/2}. \quad (8b)$$

The time derivative on the left hand side can now be exploited to solve the equation using finite difference approximation. As previously demonstrated,<sup>5</sup> we can discretize the equations in time and space separately. Since the  $\mathbf{P}$  field time derivative depends on  $\mathbf{Q}$  and  $\mathbf{P}$  fields, both equations must be solved simultaneously. This requires us to introduce an  $n + 1/2$  time step for all of the field variables.<sup>13</sup> We choose to approximate the  $\mathbf{P}$  field at the  $n + 1/2$  time step with the weighted time-averaging expression in Eq. (9), because it is known to provide greater stability at oblique incidence for lossy media.  $\beta$  is a stability factor that has been found to be optimized

at  $\frac{0.5}{\cos^2(k_z)}$ .<sup>13</sup>

$$\mathbf{P}_a^{n+1/2} = \beta \mathbf{P}_a^{n+1} + (1 - 2\beta) \mathbf{P}_a^{n+1/2} + \beta \mathbf{P}_a^n \quad (9)$$

Eq. (8) now becomes:

$$\mathbf{P}_a^{n+1} = \mathbf{P}_a^n + c\Delta t \kappa (\nabla \times \mathbf{Q}^{n+1/2}) - \alpha (\kappa \mathbf{q} \mathbf{Q}^{n+1/2} + \beta \mathbf{P}_a^{n+1} + (1 - 2\beta) \mathbf{P}_a^{n+1/2} + \beta \mathbf{P}_a^n) \quad (10a)$$

$$(\mathbf{I} + \beta \alpha) \mathbf{P}_a^{n+1} = \mathbf{P}_a^n + c\Delta t \kappa (\nabla \times \mathbf{Q}^{n+1/2}) - \alpha (\kappa \mathbf{q} \mathbf{Q}^{n+1/2} + (1 - 2\beta) \mathbf{P}_a^{n+1/2} + \beta \mathbf{P}_a^n). \quad (10b)$$

To simplify the equation we have defined a matrix  $\alpha$  such that  $\alpha = c^2 \Delta t \mu_0 \sigma'$ . This equation is true at every grid point and is independent of the choice of grid scheme, since we have made no assumptions regarding the location of grid points. However, in order to find the field values at a particular grid point, the entire matrix

equation must be discretized in terms of that grid point. We can solve for the  $\mathbf{P}^{n+1}$  field variables by inverting the matrix on the left.

The algorithm proceeds in time using Eqs. (8b) and (10b) to update the  $a$  fields from the  $\mathbf{P}$  and  $\mathbf{Q}$  fields. Once the  $\mathbf{P}_a$  and  $\mathbf{Q}_a$  variables are known, the  $\mathbf{P}$  and  $\mathbf{Q}$  fields can be calculated. We first solve for the  $z$  field components only using:

$$\mathbf{P} = (\mathbf{I} + \kappa \mathbf{q}^2)^{-1} (\mathbf{P}_a + \kappa \mathbf{q} \mathbf{Q}_a) \quad (11a)$$

$$\mathbf{Q} = (\mathbf{I} + \mathbf{q}^2)^{-1} (\mathbf{Q}_a - \mathbf{q} \mathbf{P}_a). \quad (11b)$$

Next, the  $Q_x$  and  $Q_y$  components can be found using Eq. (7b). Last, the  $P_x$  and  $P_y$  components are found using Eq. (7a). This way of solving for  $\mathbf{P}$  and  $\mathbf{Q}$ , used in previous SFM methods,<sup>13</sup> reduces spatial averaging and improves stability for our 3D orthogonal grid implementation.

### 3.2 Stability Considerations

Our FDTD algorithm is not an unconditionally stable method. The primary factor that determines stability is the Courant or stability factor. We define it using the simple lower bound for orthogonal grids found by Roden<sup>6</sup> as  $S = \frac{k_z^2}{\sqrt{2 + k_z^2}}$ . Since the our algorithm requires additional averaging needed by  $\mathbf{q}$ ,  $\epsilon$ , and  $\sigma$ , other factors will affect the stability of the algorithm besides  $S$ . This is because of the additional averaging caused by these arbitrary tensors, some of which requires the averaging of eight grid points. Therefore, we note the stability of a given simulation is dependent on most input parameters, with larger spatial differentials in parameters lowering the stability by a greater amount. For example, in general, a dielectric slab of index 2.0 placed next to vacuum will be less stable than a dielectric slab of index 1.5 placed next to vacuum. The parameters that affect the stability include index of refraction, birefringence, extinction coefficient, dichroism, and the degree of spatial uniformity. Larger angles of incidence also lower stability, due to the use of a larger magnitude of the  $\mathbf{q}$  matrix, increasing the importance of the averaged grid points. Despite these considerations, we have experimentally found our algorithm to be stable for many time steps when simulating complex anisotropic structures at large incidence angles ( $> 60^\circ$ ).

### 3.3 Implementation Considerations

To calculate broadband transmittance values, we first run a reference simulation identical to our desired simulation, but which is filled entirely with vacuum (no structure). During this simulation we capture and store the complex values of  $\mathbf{P}$  at the sampling plane (see Fig. 2). We then run the simulation containing the structure of interest and again capture and store the complex values of  $\mathbf{P}$  at the sampling plane. These field values are normalized by the reference field values to give us the transmitted field values. From here, the appropriate near-to-far field transformation can be applied to obtain far field transmittances; the sum of the far-fields yielding the total transmittance. Simply summing the intensity of the transmitted fields is not adequate to find the total transmittance, since there may be evanescent waves or trapped electrical charge present at the sampling plane.

When describing structures of interest, we many times wish to describe the optical properties in terms of the complex index of refraction  $\tilde{\mathbf{n}} = \mathbf{n} - i\kappa$ , where  $\mathbf{n}$  is the real index of refraction tensor and  $\kappa$  is the imaginary index of refraction tensor, also called the extinction coefficient. However, our algorithm is based on permittivity and conductivity. To go between the two sets of material parameters, we will equate the conductivity to the complex permittivity. The basic relationship, using Eq. (1), is:

$$\tilde{\epsilon} = \epsilon_r - j \frac{\sigma}{\omega \epsilon_0} = \tilde{\mathbf{n}}^2 = (\mathbf{n} - i\kappa)^2. \quad (12)$$

This can be solved, resulting in the desired equations:

$$\epsilon_r = \mathbf{n}^2 - \kappa^2 \quad (13a)$$

$$\sigma = 2\mathbf{n}\kappa\omega\epsilon_0. \quad (13b)$$

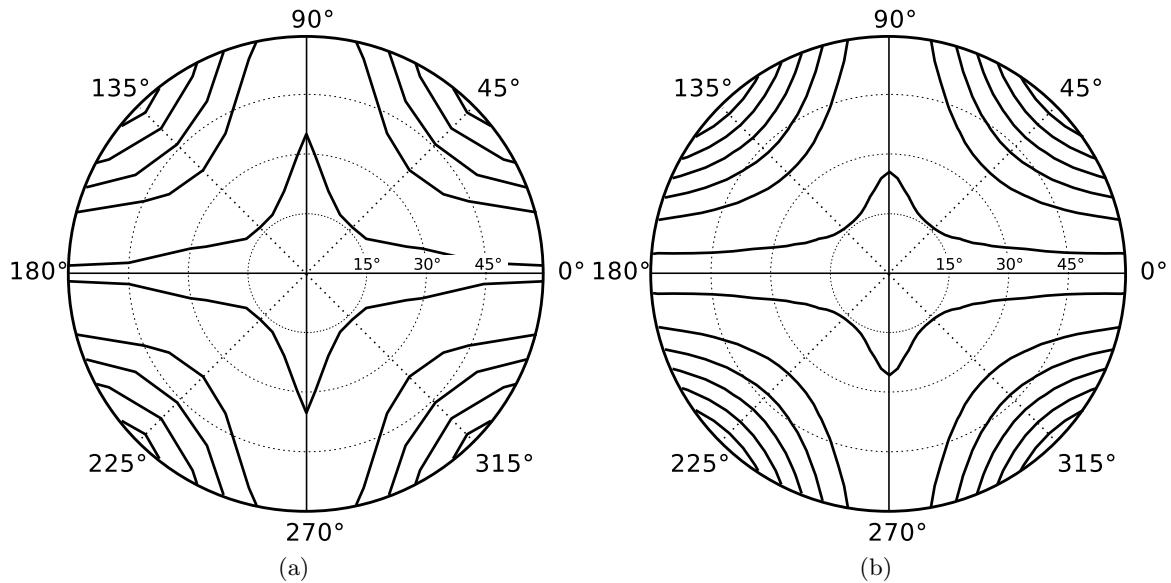


Figure 3: Conoscopic contour plot of the transmission through a pair of crossed dichroic polarizers. a) Our result. b) Berreman 4x4 result. Contour lines start at 0.001 (centermost) and increase in steps of 0.005.

## 4. VALIDATION/RESULTS

To validate our algorithm, we have implemented it in the C programming language and simulated some standard optical elements. Here we present the key results which validate that our algorithm and implementation of it are functional and stable.

### 4.1 Crossed Polarizer Pair

A pair of crossed dichroic polarizers were simulated over a range of source incidence. The first polarizer was oriented with  $T_{\parallel} = 0^\circ$  and the second polarizer was oriented with  $T_{\parallel} = 90^\circ$ . We modeled the polarizers with realistic material characteristics,<sup>14</sup> having thickness  $d = 100\mu m$ , ordinary index  $\tilde{n}_o = 1.5 - i5 \times 10^{-5}$ , and extraordinary index  $\tilde{n}_e = 1.5 - i3.1 \times 10^{-3}$ . Gradient index AR coatings were used on both sides of the polarizer pair.<sup>15</sup> The source was polarized at  $90^\circ$  and was centered at 550 nm. The angle of source incidence varied over a wide range ( $0^\circ \leq \theta \leq 60^\circ$  and  $0^\circ \leq \psi < 360^\circ$ ). The results are shown in Fig. 3a. As expected, the transmittance is the lowest at normal incidence. As the angle of incidence increases, the transmittance increases, particularly in the diagonal directions.

To validate the simulation quantitatively, we used the Berreman 4x4 method.<sup>10</sup> The Berreman method is capable of analyzing stacks of anisotropic materials, with arbitrary angle of incidence. The results of the Berreman analysis, shown in Fig. 3b, match closely with the FDTD results. The root mean square error is 0.0046, with less error at normal incidence.

### 4.2 Twisted Nematic Cell

Liquid Crystals (LCs) are one the most commonly used anisotropic materials, being present in almost every modern display. The anisotropy of the LC depends on its material phase. In the isotropic phase, an LC does not possess any anisotropy, due to the LC molecules being randomly oriented. In the nematic phase, the LC molecules become aligned to a certain direction, characterized by a vector called the nematic director. The basic LCD uses a Twisted Nematic (TN) LC cell. In the TN cell, the nematic director of the LC twists continually from one surface of the cell to the other. We can model this ideal TN cell having twist  $\phi_{twist}$  and thickness  $d$  with a permittivity tensor given by:

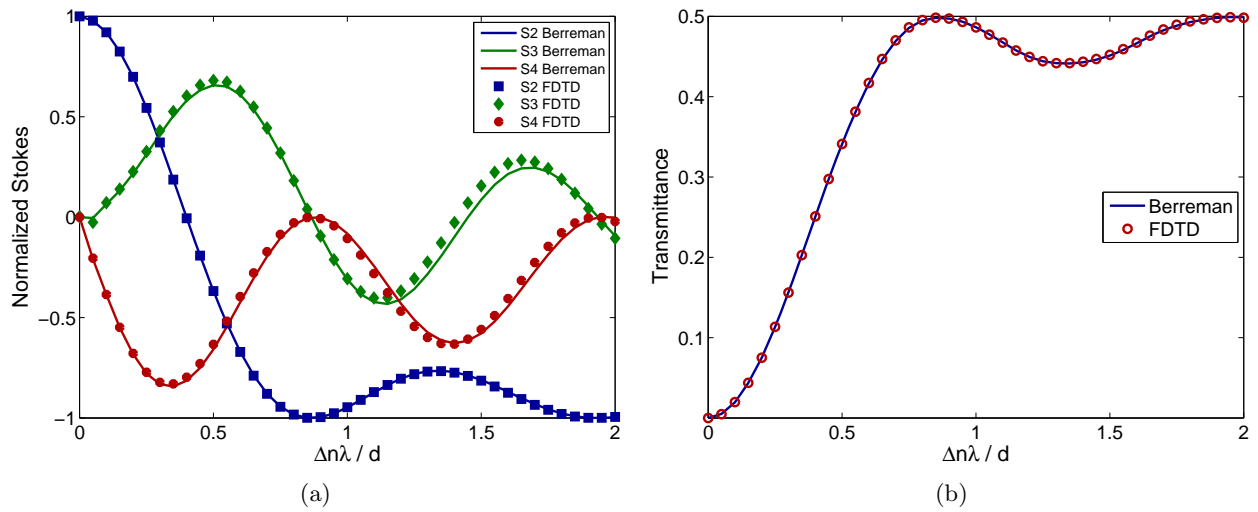


Figure 4: FDTD simulation results for an LC cell between crossed polarizers compared with Berreman 4x4. a) Normalized Stokes parameters. b) Total transmittance.

$$\epsilon = \mathbf{R}(z)^{-1} \begin{bmatrix} \epsilon_e & 0 & 0 \\ 0 & \epsilon_o & 0 \\ 0 & 0 & \epsilon_o \end{bmatrix} \mathbf{R}(z) \quad (14)$$

where  $\mathbf{R}(z)$  is a rotation matrix given by:

$$\mathbf{R}(z) = \begin{bmatrix} -\sin(\frac{z}{d}\phi_{twist}) & \cos(\frac{z}{d}\phi_{twist}) & 0 \\ \cos(\frac{z}{d}\phi_{twist}) & \sin(\frac{z}{d}\phi_{twist}) & 0 \\ 0 & 0 & 1 \end{bmatrix}. \quad (15)$$

We simulated a lossless TN cell having properties  $n_o = 1.5$ ,  $n_e = 1.6$ ,  $d = \frac{\lambda}{2\Delta n}$  for  $\lambda = 550nm$ , and  $\phi_{twist} = 90^\circ$ . AR coatings are placed on either side of the cell. We avoid simulating the substrates for simplicity. The stokes parameters of the transmitted light are shown in Fig. 4a, and the total transmittance is shown in Fig. 4b. Also shown are the Berreman 4x4 results of the same TN cell. The stokes parameters indicate that the polarization properties of the transmitted light vary dramatically with wavelength, as expected. Both the stokes and total transmittance results produced by the FDTD simulation are very close to those predicted by the Berreman 4x4, as well as derived equations for the transmittance.<sup>16</sup>

### 4.3 2D Array of Conducting Particles

There is great interest in 2D arrays of subwavelength conducting or semiconducting particles, for use as optical filters, detectors, photonic couplers, and more. We simulate light incident upon such an array of perfectly conducting particles. With the right parameters, the particle array will reflect incidence light of a certain wavelength with 100% efficiency. The particles simulated are rectangular and of equal height and width, with a width of  $\Lambda/5$ , where  $\Lambda$  is the period. The period is the same for both  $x$  and  $y$  dimensions. The geometry is shown in Fig. 5a. We set  $\Lambda = 1\mu m$  and chose a thickness  $d = 0.05\mu m$ . Since we are employing periodic boundaries, we only need simulate one period of the system. We model the perfect electric conductors by setting the conductivity to a sufficiently high value. We plot the reflectance in Fig. 5b. The spectra contains the expected 100% reflectance peak. The wavelength at which the peak occurs, as well as the shape of the transmittance function agree with previous experimental and numerical results for similar structures.<sup>17</sup> We also

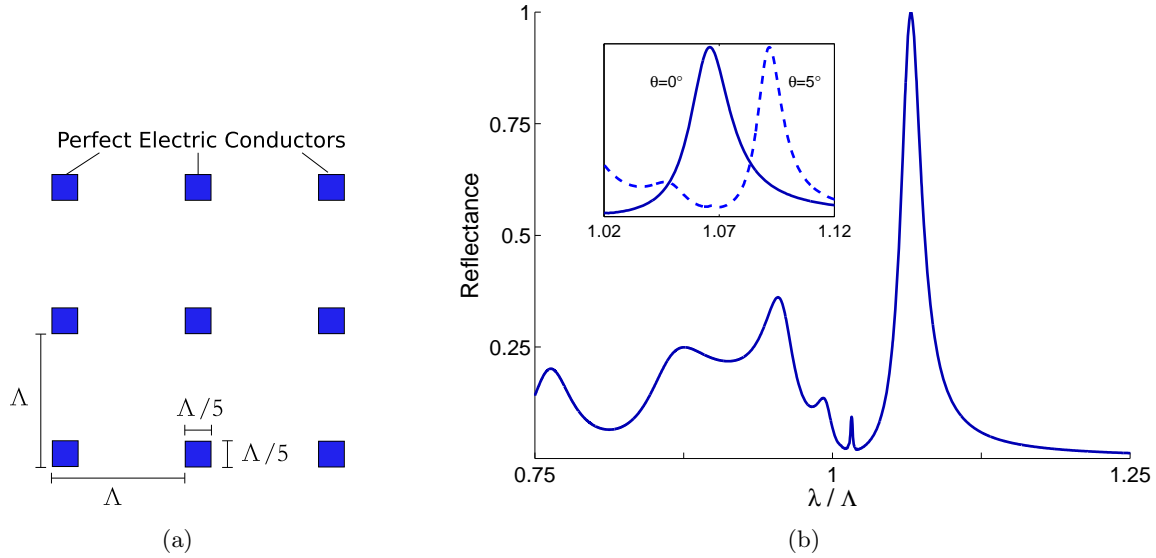


Figure 5: a) The geometry of the infinite 2D array of square perfect electric conductor particles. b) Reflectance through the 2D array. Inset: a close up of the 100% reflectance maxima for normal incidence and  $\phi = 45^\circ$  and  $\theta = 5^\circ$ .

simulate the array at an incidence of  $\phi = 45^\circ$  and  $\theta = 5^\circ$ , shown in the Fig. 5b inset. As expected, the location of maximum reflectance shifts by a slight amount.

#### 4.4 Polarization Grating

As stated in Section 1, PGs are unique diffractive optical elements capable of diffracting light to a single order with theoretical 100% efficiency, which we will denote here as  $\eta_{+1}$ .<sup>11</sup> The diffraction is polarization sensitive, with circular light of one handedness being diffracted to the +1 order, circular light of the opposite handedness being diffracted to the -1 order, and linear light being diffracted to both the +1 and -1 orders. In order to achieve  $\eta_{+1} = 1$ , the PG should be half-wave thickness for the desired wavelength. With this in mind, a PG can be thought of as a traditional birefringent half-wave plate with a optical axis that continually rotates across the structure. A full revolution of the optical axis defines one period,  $\Lambda$ , of the structure. The direction of the diffracted light follows the well known diffraction equation. PGs are useful for a wide range of applications, including beam steering,<sup>18</sup> polarization conversion systems,<sup>19</sup> and tunable optical filters.<sup>20</sup>

PGs have been simulated with FDTD and oblique incidence before.<sup>21</sup> However, this modeling was 2D and therefore only capable of in-plane oblique incidence, i.e.  $\phi = 0^\circ$  with a grating vector directed in  $\phi = 0^\circ$ . We here for the first time simulate a PG with arbitrary angle of source incidence, specifically the  $\phi = 90^\circ$  or out-of-plane case. We also show the  $\phi = 0^\circ$  case in the figures for comparison. The PG simulated has index  $n = 1.5$ , birefringence  $\Delta n = 0.2$ , thickness  $d = \lambda/2\Delta n$ , and period  $\Lambda = 5\lambda$ . The grating vector was in the  $\phi = 0^\circ$  direction and the source was right-hand circular polarized. Fig. 6 shows the results of our simulations. The results follow the general trends seen with the  $\phi = 0^\circ$  case,<sup>21</sup> but there are significant differences.

In Fig. 6a we show the broadband response with angles of incidence  $\theta = 0^\circ$  and  $\theta = 50^\circ$  for  $\phi = 0^\circ$  and  $\phi = 90^\circ$ . With any angle of incidence,  $\eta_{+1}$  is decreased while  $\eta_0$  and other orders (not shown) are increased. However, it is clear from the figure that the diffraction efficiency is much more effected by in-plane incidence than out-of-plane incidence. Concerning the broadband response characteristics, we note that for  $\phi = 90^\circ$  the location of the diffraction maxima and minima shift only slightly, while  $\phi = 0^\circ$  shifts them a noticeable amount.

Fig. 6b shows the progression of  $\eta$  with incidence angle, for both the  $\phi = 0^\circ$  and  $\phi = 90^\circ$  cases, for a single wavelength,  $\lambda = 2\Lambda nd$ . Concerning the  $\phi = 90^\circ$  case,  $\eta_{+1}$  decreases in an exponential manner, but at a very slow pace compared to in-plane incidence. The decreases in  $\eta_{+1}$  are insignificant up to around  $10^\circ$ , after which  $\eta_0$ ,  $\eta_{+2}$  (not shown), and  $\eta_{-1}$  (not shown) increase with similar magnitude at the expense of  $\eta_{+1}$ . When compared



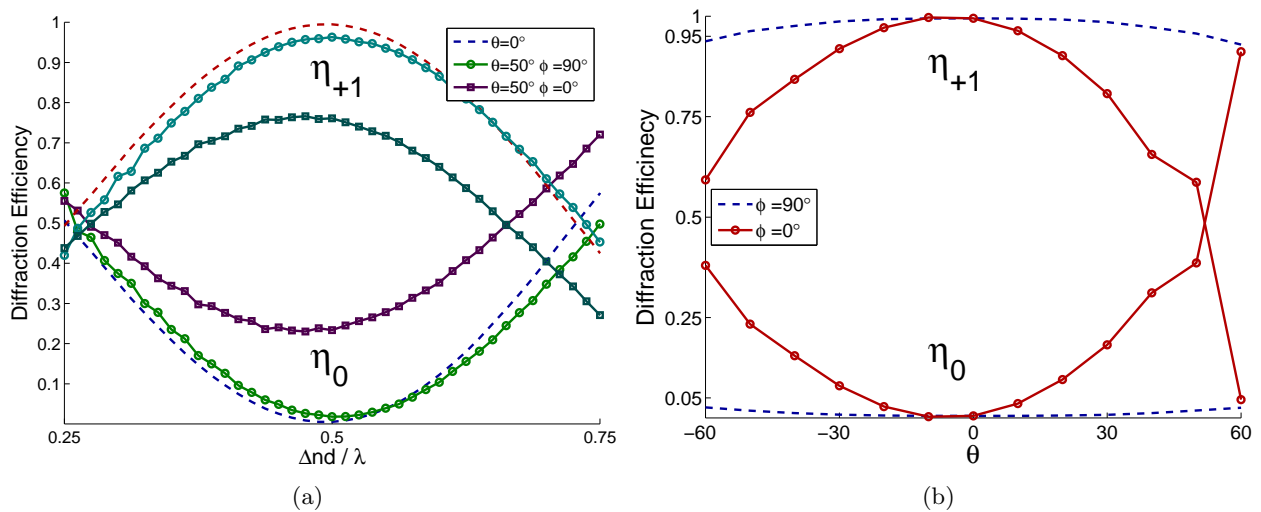


Figure 6: a) PG diffraction efficiencies (%) for the +1 and 0 order over a range of wavelengths, for  $\theta = 0^\circ$  and  $50^\circ$  for  $\phi = 90^\circ$ . b) PG diffraction efficiencies (%) for the 0, +1, and +2 orders for  $\theta = 0^\circ$  through  $60^\circ$  for  $\phi = 90^\circ$ .

to the  $\phi = 0^\circ$  case, the  $\phi = 90^\circ$  case has a much higher  $\eta_{+1}$  even at low angles of incidence. We also note that the results are not symmetric around normal incidence, similar to the  $\phi = 0^\circ$  case.

From this data, we can conclude that the diffraction efficiency of a PG is sensitive to out-of-plane incidence, but not nearly as sensitive as it is to in-plane incidence. From here, we can begin to quantify arbitrary angle of incidence on PG diffraction efficiency. Such information will be a valuable aid in the design of PG based systems and devices.

## 5. CONCLUSIONS

A powerful FDTD algorithm is presented based upon the full tensor description of permittivity and conductivity in Maxwell's equations and the SFM. By including the full tensors in Ampere's law, we are able to implement a powerful tool that can simulate nearly any three dimensional device that can be described in terms of permittivity and conductivity. By combining this descriptive capability with the SFM, we can simulate off-axis plane wave sources. We implemented and validated our algorithm through several simulations with known results, and simulated a PG with out-of-plane incidence for the first time. The algorithm developed in this paper gives us a powerful tool with which to analyze complex inhomogeneous structures with arbitrary anisotropic non-magnetic materials.

## ACKNOWLEDGMENTS

The authors gratefully acknowledge the support of the National Science Foundation (NSF grant ECCS-0955127).

## REFERENCES

- [1] Yee, K. S., "Numerical solution of initial boundary value problems involving maxwell's equations in isotropic media," *IEEE Trans. Antennas Propag.* **14**, 302–307 (1966).
- [2] Holland, R., "Finite-Difference solution of maxwell's equations in generalized nonorthogonal coordinates," *IEEE Trans. Nucl. Sci.* **30**(6), 4589–4591 (1983).
- [3] Gedney, S. D., "An anisotropic perfectly matched layer absorbing medium for the truncation of fdtd lattices," *IEEE Trans. Antennas Propag.* **44**, 1630–1639 (1996).
- [4] Young, J. L. and Nelson, R. O., "A summary and systematic analysis of FDTD algorithms for linearly dispersive media," *IEEE Trans. Antennas Propag.* **43**(1), 61–77 (2001).

- [5] Schneider, J. and Hudson, S., "The finite-difference time-domain method applied to anisotropic material," *IEEE Trans. Antennas Propag.* **41**(7), 994 (1993).
- [6] Roden, J. A., Gedney, S. D., Kesler, M. P., Maloney, J. G., and Harms, P. H., "Time-domain analysis of periodic structures at oblique incidence: orthogonal and nonorthogonal fdtd implementation," *IEEE Trans. Microw. Theory Tech.* **46**, 420–427 (1998).
- [7] Oh, C. and Escuti, M. J., "Time-domain analysis of periodic anisotropic media at oblique incidence: an efficient fdtd implementation," *Opt. Exp.* **14**(24), 1870–1884 (2006).
- [8] Belkhir, A. and Baida, F. I., "Three-dimensional finite-difference time-domain algorithm for oblique incidence with adaptation of perfectly matched layers and nonuniform meshing: application to the study of a radar dome," *Phys. Rev. E* **77** (2008).
- [9] Yeh, P., "Extended jones matrix-method," *J. Opt. Soc. Am.* **72**(4), 507–513 (1982).
- [10] Berreman, D. W., "Optics in stratified and anisotropic media - 4X4-matrix formulation," *J. Opt. Soc. Am.* **62**(4), 502–& (1972).
- [11] Nikolova, L. and Todorov, T., "Diffraction efficiency and selectivity of polarization holographic recording," *Opt. Acta* **31**, 579–588 (1984).
- [12] Arfken, G. B. and Weber, H. J., [*Mathematical methods for physicists*], Academic Press, San Diego (1995).
- [13] Taflove, A., [*Computational electrodynamics: the finite-difference time-domain method*], Artech House, Boston (1995).
- [14] Haas, G., Wohler, H., Fritsch, M., and Mlynski, D. A., "Polarizer Model For Liquid-Crystal Devices," *J. Opt. Soc. Am. A-Opt. Image Sci. Vis.* **5**(9), 1571–1575 (1988).
- [15] Southwell, W. H., "Gradient-Index anti-reflection coatings," *Opt. Lett.* **8**(11), 584–586 (1983).
- [16] Gooch, C. H. and Tarry, H. A., "Optical-properties of twisted nematic liquid-crystal structures with twist angles less than 90 degrees," *Journal Of Physics D-Applied Physics* **8**(13), 1575–1584 (1975).
- [17] de Abajo, F. J. G., "Colloquium: Light scattering by particle and hole arrays," *Rev. Mod. Phys.* **79**(4), 1267–1290 (2007).
- [18] Kim, J., Oh, C., Serati, S., and Escuti, M. J., "Wide-angle, nonmechanical beam steering with high throughput utilizing polarization gratings," *App. Opt.* **50**(17), 2636–2639 (2011).
- [19] Kee, E. S. H. C., Kim, Y., Jeong, S., Choi, H., Lee, S., Kim, J., Komanduri, R. K., and Escuti, M. J., "Polarization conversion system using a polymer polarization grating," *SID Symposium Digest* **42**, 540–543 (2011).
- [20] Nicolescu, E. and Escuti, M. J., "Polarization-independent tunable optical filters using bilayer polarization gratings," *App. Opt.* **49**(20), 3900–3904 (2010).
- [21] Oh, C. and Escuti, M. J., "Numerical analysis of polarization gratings using the finite-difference time-domain method," *Phys. Rev. A* **76**(4) (2007).